

XMM/HST monitoring of the ultra-soft highly accreting Narrow Line Seyfert 1 RBS 1332

R. Middei^{1,2,*}, S. Barnier³, F. G. Saturni^{1,2}, F. Ursini⁵, P.-O. Petrucci⁴, S. Bianchi⁵, M. Cappi⁶, M. Clavel⁴, B. De Marco⁷, A. De Rosa⁸, G. Matt⁵, G. A. Matzeu⁹, and M. Perri^{1,2}

¹ INAF Osservatorio Astronomico di Roma, Via Frascati 33, 00078 Monte Porzio Catone (RM), Italy.

² Space Science Data Center, Agenzia Spaziale Italiana, Via del Politecnico snc, 00133 Roma, Italy.

³ Department of Earth and Space Science, Graduate School of Science, Osaka University, Toyonaka, Osaka 560-0043, Japan.

⁴ Univ. Grenoble Alpes, CNRS, IPAG, 38000 Grenoble, France.

⁵ Dipartimento di Matematica e Fisica, Università degli Studi Roma Tre, Via della Vasca Navale 84, 00146 Roma, Italy.

⁶ INAF-Osservatorio di Astrofisica e Scienza dello Spazio di Bologna, Via Gobetti, 93/3, 40129 Bologna, Italy.

⁷ Departament de Física, EEBE, Universitat Politècnica de Catalunya, Av. Eduard Maristany 16, 08019 Barcelona, Spain.

⁸ INAF, Istituto di Astrofisica e Planetologia Spaziali, Via Fosso del Cavaliere, 100 - I-00133 Rome, Italy.

⁹ Quasar Science Resources SL for ESA, European Space Astronomy Centre (ESAC), Science Operations Department, 28692, Villanueva de la Cañada, Madrid, Spain.

Received mm/dd/yyyy; accepted mm/dd/yyyy

ABSTRACT

Ultra-soft narrow line Seyfert 1 (US-NLSy) are a poorly observed class of active galactic nuclei characterized by significant flux changes and an extreme soft X-ray excess. This peculiar spectral shape represents a golden opportunity to test whether the standard framework commonly adopted for modelling local AGN is still valid. We thus present the results on the joint *XMM-Newton* and *HST* monitoring campaign of the highly accreting US-NLSy RBS 1332. The optical-to-UV spectrum of RBS 1332 exhibits evidence of both a stratified narrow-line region and an ionized outflow, that produces absorption troughs over a wide range of velocities (from ~ 1500 km s⁻¹ to ~ 1700 km s⁻¹) in several high-ionization transitions (Ly α , N V, C IV). From a spectroscopic point of view, the optical/UV/FUV/X-rays emission of this source is due to the superposition of three distinct components which are best modelled in the context of the two-coronae framework in which the radiation of RBS 1332 can be ascribed to a standard outer disk, a warm Comptonization region and a soft coronal continuum. The present dataset is not compatible with a pure relativistic reflection scenario. Finally, the adoption of the novel model `REXCOR` allowed us to determine that the soft X-ray excess in RBS 1332 is dominated by the emission of the optically thick and warm Comptonizing medium, and only marginal contribution is expected from relativistic reflection from a lamppost-like corona.

Key words. galaxies: active – galaxies: Seyfert – X-rays: galaxies – X-rays: individual: RBS 1332

1. Introduction

Active galactic nuclei (AGN) are compact sources at the center of galaxies. They are powered by accretion of matter onto a supermassive black hole and emit across the whole electromagnetic domain, from radio up to γ -rays (e.g. Padovani et al. 2017).

AGN are characterized by a significant amount of energy emitted in the optical/UV and X-ray ranges. This emission is accounted for by the so-called two phase model (Haardt & Maraschi 1991, 1993). Seed optical/UV photons from an optically thick geometrically thin accretion disc are Compton scattered to the X-rays by a thermal distribution of electrons, the so-called hot corona. This mechanism explains the power-law shape of the X-ray spectrum and the observations of a high-energy cut-off at a few hundred keV in most sources (Perola et al. 2000; Malizia et al. 2014; Fabian et al. 2015; Tortosa et al. 2018; Kamraj et al. 2022). The reprocessing of the primary X-ray continuum by the disc or more distant material gives rise to features like a Fe K α emission line (e.g. George & Fabian 1991). Most objects also show the presence of a soft X-ray excess, below ~ 2 keV, with respect to the high-energy power-law extrapolation

(e.g. Bianchi et al. 2009; Gliozzi & Williams 2020).

The physical origin of this soft X-ray excess component is still highly debated. So far, two models have been commonly adopted to describe such a component: relativistic reflection and warm Comptonization. In the first case, it is assumed that the soft X-ray excess results from the blending of emission lines due to relativistic reflection (e.g. Crummy et al. 2006). On the other hand, an alternative explanation invokes an additional emitting component, the so-called warm corona, which is described as an optically thick and geometrically thin warm plasma above the accretion disc (e.g. Magdziarz & Zdziarski 1995; Petrucci et al. 2013). This component can be modeled as fully covering the accretion disc (the disc in this case is assumed to be passive Petrucci et al. 2018), or as a patchy medium (Kubota & Done 2018), partially covering the accretion disc. From an observational X-ray perspective, the soft excess of AGN have been successfully reproduced using a pure relativistic reflection scenario (Walton et al. 2013; Mallick et al. 2018; Jiang et al. 2020; Xu et al. 2021). The analysis of multiwavelength multi-epoch datasets proved to be a powerful tool for studying the origin of the soft X-ray excess. A broadband coverage enables us to model and disentangle the different spectral components and, through

* riccardo.middei@ssdc.asi.it

variability, test the connection among them (Middei et al. 2023; Mehdipour et al. 2023). In these cases, the joint fit of the UV and X-ray data shows that warm Comptonization is a viable model to explain the origin of the soft X-ray excess and is generally statistically favored by the data compared to a pure relativistically blurred reflection model (e.g. Matzeu et al. 2020; Middei et al. 2020; Porquet et al. 2021, 2024).

In the context of this approach, we complemented our previous spectral and variability campaigns with a new series of *XMM-Newton* and *HST* observations of RBS 1332 ($z=0.122$, Bade et al. 1995). This source is classified as an Ultra Soft Narrow Line Seyfert 1 (US-NLSy 1), AGN potentially hosting BHs accreting around or above the Eddington limit, and with inner disc regions characterized by higher temperatures with respect to standard Seyfert galaxies. In particular, the disc emission is expected to peak in the Far Ultra Violet (FUV) rather than in the UV. They are also characterised by strong Fe II emission (e.g. Osterbrock 1977; Goodrich 1989). In the X-rays, they exhibit a much steeper continuum in comparison with average Seyferts (i.e. Γ in the range 2.0-2.5 instead of 1.5-2, e.g. Bianchi et al. 2009), and a strong, highly variable soft excess (Gallo 2018). The origin of their broadband continuum is still debated. In fact, although Jiang et al. (2020) successfully modelled the *XMM-Newton* data of five US-NLSys with relativistic blurred reflection model, for at least one of these sources (RX J0439.6-5311) the two-coronae model was found to provide also a good fit (Jin et al. 2017a,b). RBS 1332 has very low intrinsic absorption ($E_{B-V} = 0.008$ Grupe et al. 2010), making it ideal for studying the relation between the soft X-ray band and UVs and Grupe et al. (2004) reported on the optical properties of this NLSy1 source with $\text{FWHM}(H\beta)=1100 \text{ km s}^{-1}$ and a $H\alpha/H\beta \sim 3.3$. In this paper we will thus test the origin of the soft X-ray excess in RBS 1332 studying a broadband multi-epoch dataset taken with *XMM-Newton* and *HST*. The paper is organised as follows: The data reduction is discussed in Sect. 2; Sect.s 3 and 4 report on the UV and UV-to-X-ray spectral analysis, respectively. Finally, in Sect. 5 we discuss and comment on our findings.

2. Data processing and reduction

The RBS 1332 data analysed here belongs to the joint *XMM-Newton/HST* observational campaign consisting in $5 \times (20 \text{ ks (XMM-Newton)} + 1 \text{ orbit (HST)})$ quasi-simultaneous observations. The exposures cover the time period between November 06th and 19th 2022, with consecutive pointings being about two or three days apart, see Table 1. Unfortunately, due to star tracker errors, *HST* was unable to observe during epochs 2 and 3.

XMM-Newton data of RBS 1332 were obtained with the EPIC cameras (Strüder et al. 2001; Turner et al. 2001) in Small Window mode with the medium filter applied. Science products are obtained processing the *XMM-Newton* Science Analysis System (SAS, Version 21.0.0). The source extraction radius and the screening for high background time intervals were executed adopting an iterative process that maximizes the S/N (as described in Piconcelli et al. 2004; Nardini et al. 2019). The source radii span between 29 and 34 arcsec, while the background was computed from a blank region with radius 40 arcsec. Spectra are later binned to have at least 30 counts in each bin, and not to oversample the instrumental energy resolution by a factor larger than 3. We also extract data provided by the Optical Monitor (Mason et al. 2001), on-board *XMM-Newton*. RBS 1332 was observed with the filters UVW1 (2910 Å), UVM2 (2310 Å), UVW2 (2120 Å) during the whole monitoring program. Data provided by the OM were extracted using the standard proce-

Table 1. Log of the observations *XMM-Newton-HST* monitoring campaign.

Observatory	Obs. ID	Start date yyyy-mm-dd	Net exp. ks
<i>XMM-Newton</i>	0903370201	2022-11-06	~22
<i>HST</i>		2022-11-06	~2
<i>XMM-Newton</i>	0903370301	2022-11-09	~23
<i>XMM-Newton</i>	0903370401	2022-11-12	~24
<i>XMM-Newton</i>	0903370501	2022-11-15	~30
<i>HST</i>		2022-11-16	~2
<i>XMM-Newton</i>	0903370601	2022-11-18	~25
<i>HST</i>		2022-11-19	~2

dure within SAS and we converted the spectral points into an XSPEC (Arnaud 1996) compliant format using the task `om2PHA`.

In Fig. 1 we show the soft (0.3-2 keV) and hard (2-10 keV) light curves (top and middle panels) and their ratios (bottom panels). In accordance with this figure, flux variability of up to 30% on hourly timescale is observed. On very short timescales (of a few ks), the hardness ratios show hints of mild spectral variability, especially in the final part of pointing 2 and for about ~6 ks in observation 5. However, the short duration of these events does not allow us to obtain a sufficiently high S/N for a detailed time-resolved analysis, therefore we decided to average over the entire exposures.

RBS 1332 was also observed by the Hubble Space Telescope using the Cosmic Origins Spectrograph (COS). This spectrograph (Green et al. 2012) enables to perform high-sensitivity, medium- and low-resolution (1500–18000) spectroscopy in the 815–3200 Å wavelength interval. In this case, grating G140L centered at 1280 Å was adopted, thus enabling us to measure the source emission between 1100 and 2280 Å (observer frame). Final spectra were obtained through the automatic *HST*/COS calibration pipeline CalCOS.

In Fig. 2 we show the OM and COS rates as observed by *XMM-Newton* and the *HST* telescope. Differently to the X-rays flux, no significant flux evolution is observed in optical/UV during the observational campaign.

3. HST analysis

We started our investigation on the broadband properties of RBS 1332 characterizing its *HST* spectrum. First, we visually inspected the main UV emission lines in search of relevant absorption features. In doing this, we found that the Ly α , the N V and the C IV transitions were affected by absorption. The position and shape of each trough are similar in all the emission features, with only the “red” Ly α absorption missing. This hints at the fact that such absorption features are produced by material intrinsic to RBS 1332 that is located in the surrounding environment of the AGN central engine; to accurately quantify its properties, we performed a spectral decomposition of every absorbed emission system.

We show the Ly α +N V and C IV spectral regions of each observation in Fig. 3: at a glance, all absorption features appear to be relatively stable in both shape and depth within the spectral noise over the three *HST* epochs (see Tab. 1). This implies that the absorber is neither changing in structure (e.g., Krongold et al. 2010; Hall et al. 2011) nor responding to variations in the ionizing flux (e.g., Barlow et al. 1992; Trevese et al. 2013) over the course of the *HST* observations; this allowed us to combine them together by averaging them into a single UV spectrum in

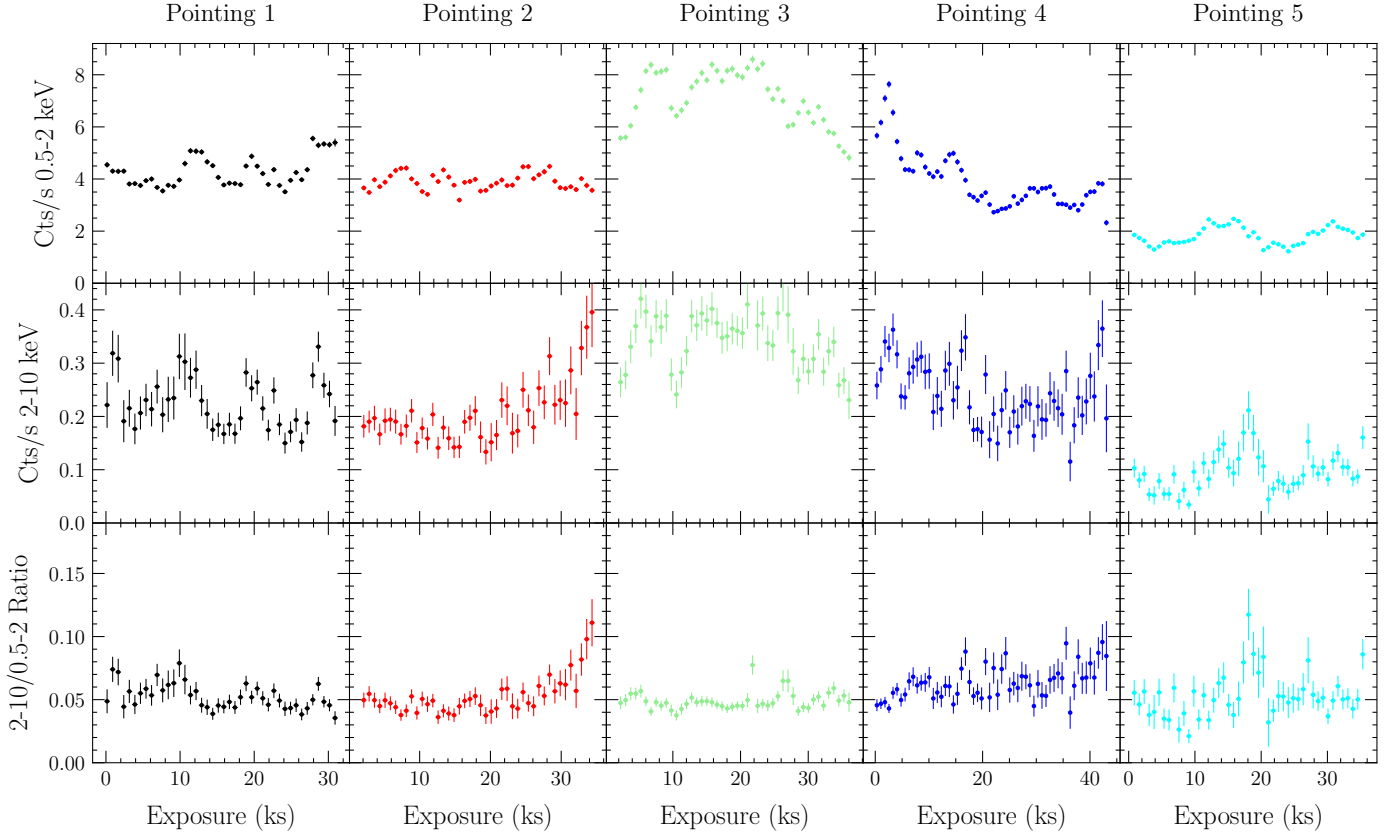


Fig. 1. Multi-epoch X-ray time series of RBS 1332. The soft X-rays show a significant variability compatible with flux changes observed above 2 keV. The ratios between hard and soft X-rays also exhibit changes on ks timescales, especially in observations 2 and 5, see the Sect. 2 for model details. Black, red, green, blue, magenta and cyan colours refer to obs. 1, obs. 2, obs. 3, obs. 4 and obs. 5, respectively. This color code is adopted in the whole paper.

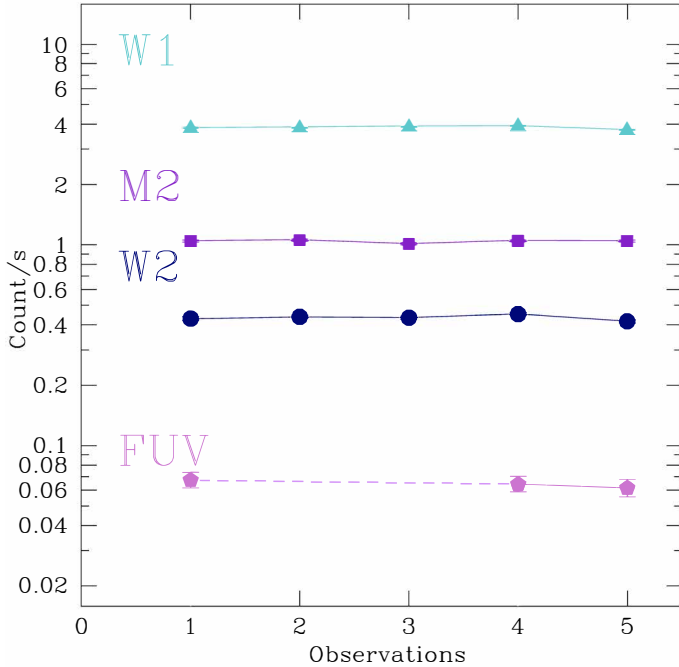


Fig. 2. UV light-curves obtained using XMM-Newton optical monitor and HST (FUV).

the observer-frame interval 1110–2280 Å (corresponding to an interval 990–2030 Å in the rest frame). On this spectrum, we

identified intervals that are relatively free of major emission and absorption features, and used them to compute a power-law continuum F_λ of the form:

$$F_\lambda \propto \lambda^\alpha \quad (1)$$

with α the spectral index. The result fits well the RBS 1332 continuous emission over the entire wavelength interval, with $\alpha = -1.37 \pm 0.10$; therefore, we adopt this fit as a good representation of the actual RBS 1332 continuum in the following analysis of the AGN emission and absorption lines.

During this step, we also identified the presence of two strong emission features blueward of the Ly α ; the most intense one falls at the Ly α rest-frame wavelength of 1215.67 Å, whereas the position of the second one is compatible with that of the O I + Si II system (Vanden Berk et al. 2001). A visual inspection revealed that such features are single Gaussian-like lines rather than being formed by multiple components. These lines are present in all the three *HST* exposures, and are due to airglow emission originated as part of the UV sky background¹; since they are not relevant for the RBS 1332 spectral analysis, we masked, thus excluded, them from any calculation. The RBS 1332 average *HST* spectrum is shown in Fig. 4.

We adopted the power-law shape found in Sect. 3 as our fiducial continuum over the entire spectral interval; on top of this component, we fitted the emission lines using multiple Gaussians:

¹ See <https://hst-docs.stsci.edu/cosihb/chapter-7-exposure-time-calculator-etc/7-4-detector-and-sky-backgrounds>.

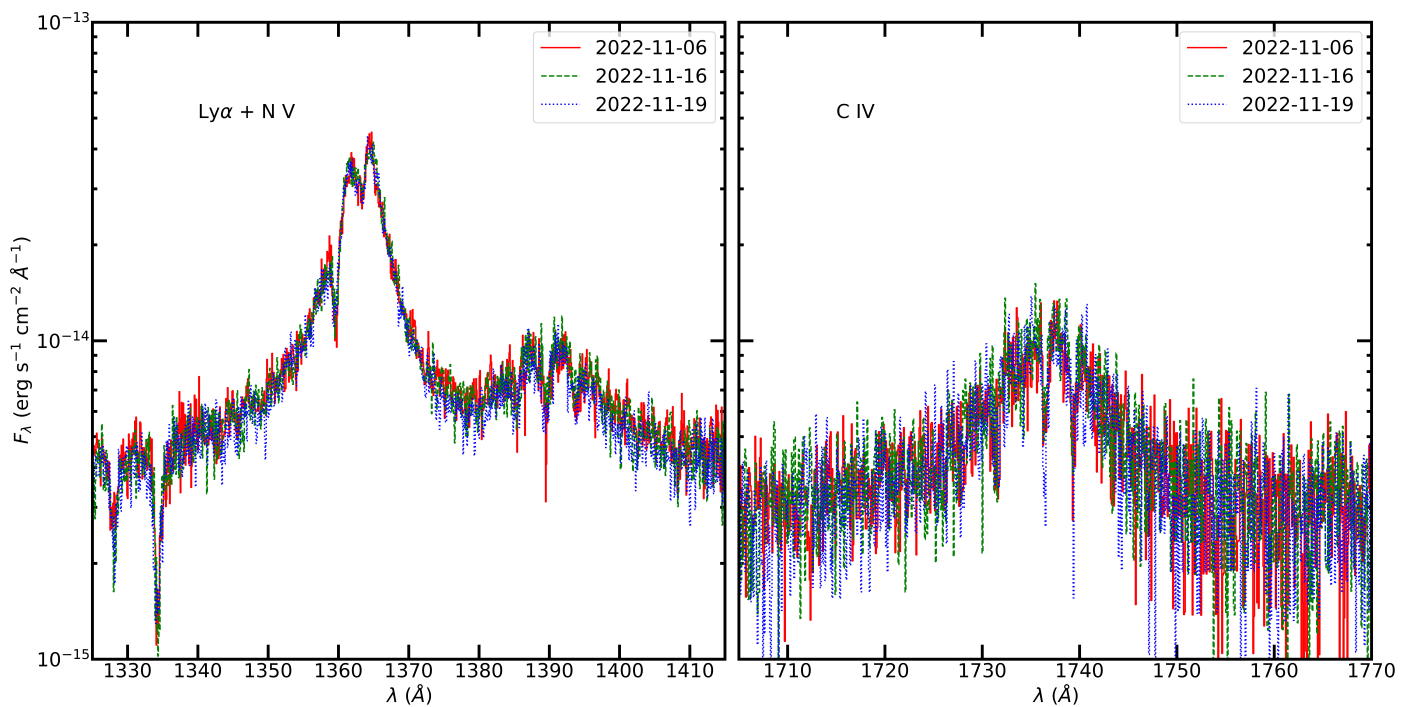


Fig. 3. Comparison of the RBS 1332 Ly α +N v and C IV spectral regions in the observer frame over the three *HST* observation epochs (see legend). *Left panel:* Ly α +N v spectral region. *Right panel:* C IV spectral region.

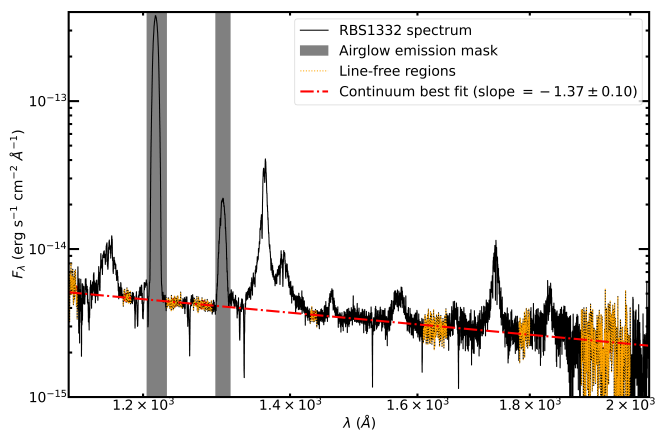


Fig. 4. HST spectrum of RBS 1332 (black solid line). The continuum emission (red dot-dashed line) fitted over intervals free of major emission and absorption features (yellow dotted lines) is indicated, along with the masks (grey bands) superimposed to the emission of the UV airglow lines.

- a narrow and a broad component for both the Ly α and the C IV;
- a single broad component for the N V;

For all components, we left all the parameters free to vary; the goodness of each performed fit was evaluated by computing the χ^2 value and the associated degrees of freedom number $\nu_{d.o.f.}$. The result of such fits is shown in Fig. 5, the obtained parameters of the line components are reported in Tab. 2.

It is immediate to note from Tab. 2 and Fig. 5 that we did not find evidence of narrow emission components ($\sigma < 600 \text{ km s}^{-1}$) in any of the analyzed transitions. This feature is often found in objects that lie at the bright end of the AGN luminosity function

Table 2. Best-fit parameters of the RBS 1332 Ly α , N v and C IV emission lines, along with the associated 1σ uncertainties.

Parameter	Ly α	N v	C IV	Units
F_1	4.27 ± 0.14	1.22 ± 0.06	1.20 ± 0.24	$10^{-12} \text{ erg s}^{-1} \text{ cm}^{-2}$
F_2	1.41 ± 0.04	—	0.54 ± 0.08	$10^{-12} \text{ erg s}^{-1} \text{ cm}^{-2}$
Δv_1	-230 ± 30	-30 ± 30	-490 ± 130	km s^{-1}
Δv_2	-30 ± 10	—	-60 ± 30	km s^{-1}
σ_1	2190 ± 40	1300 ± 30	1830 ± 160	km s^{-1}
σ_2	610 ± 10	—	670 ± 40	km s^{-1}

(see e.g. Saturni et al. 2018, and refs. therein); in such cases, forbidden transitions – such as the [O III] $\lambda 4959,5007$ doublet – tend to be weak, and an anti-correlation between their intensities and blended Fe II emission (Boroson & Green 1992) is also expected. To investigate the possible weakness of the [O III] $\lambda 4959,5007$ we retrieved the RBS 1332 optical spectrum from the SDSS Data Release 16 (DR16; Blanton et al. 2017) portal², and inspected the H β + [O III] spectral region: the [O III] is clearly detected, with both a line width typical of narrow-line regions (NLRs; $\sigma \sim 250 \text{ km s}^{-1}$) and the evidence of a blue-shifted broader component, also indicative of the presence of an outflow similar to those discovered in other nearby AGN such as IRAS 20210+1121 (Saturni et al. 2021). Due to these findings, we conclude that the lack of narrow components in the high-ionization emission lines of RBS 1332 must be ascribed to other physical phenomena, e.g. a lowly ionized or stratified NLR (e.g., Wang & Xu 2015).

² Available at <https://skyserver.sdss.org/dr16/en/tools/quicklook/summary.aspx>.

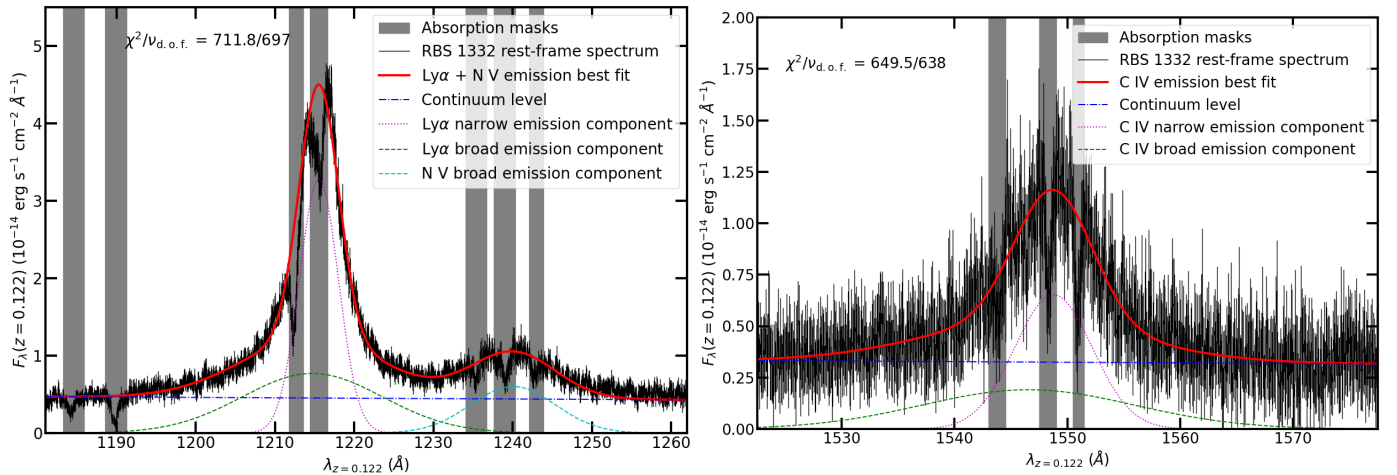


Fig. 5. *Left panel:* fit to the Ly α +N v emission system of RBS 1332 (*see insert*). *Right panel:* fit to the C IV emission (*see insert*). In both panels, the main absorption features identified through visual inspections (*grey bands*) are masked.

3.1. AGN physical parameters of RBS 1332

From the decomposition of the RBS 1332 UV spectrum, we derived all of the physical quantities that describe the AGN central engine. All the results of this paragraph are summarized in Tab. 3, along with the corresponding 1σ statistical uncertainties. We first computed the monochromatic luminosities at 1350 Å $\lambda L_{\lambda}(1350 \text{ \AA})$ and at 1450 Å $\lambda L_{\lambda}(1450 \text{ \AA})$ by integrating the RBS 1332 spectrum in 100-Å wide intervals centered around the rest-frame wavelength of interest; then, we used the C IV relation by Vestergaard & Peterson (2006) to derive the SMBH mass M_{BH} from $\lambda L_{\lambda}(1350 \text{ \AA})$ and the FWHM of the narrower component of the C IV emission line:

$$\log\left(\frac{M_{\text{BH}}}{M_{\odot}}\right) = 6.66 + 2 \log\left(\frac{\text{FWHM}_{\text{CIV}}}{1000 \text{ km s}^{-1}}\right) + 0.53 \log\left[\frac{\lambda L_{\lambda}(1350 \text{ \AA})}{10^{44} \text{ erg s}^{-1}}\right] \quad (2)$$

In doing so, we note that our estimate of M_{BH} is fully compatible within the uncertainties with the SDSS DR16Q measurement of $(2.2^{+1.5}_{-0.9}) \times 10^7 M_{\odot}$ (Wu & Shen 2022, *see* Tab. 3); therefore, we decided to adopt it as our fiducial value without applying the correction by Denney (2012) for C IV outflow-induced biases³. From the M_{BH} derived in this way, we estimated the Eddington luminosity L_{Edd} of RBS 1332. Subsequently, we adopted the relation by Runnoe et al. (2012b,a) to compute the AGN bolometric luminosity L_{bol} from $\lambda L_{\lambda}(1450 \text{ \AA})$:

$$L_{\text{bol}} = 0.75 \times 10^{4.745} [\lambda L_{\lambda}(1450 \text{ \AA})]^{0.910} \quad (3)$$

and thus the Eddington ratio $\varepsilon_{\text{Edd}} = L_{\text{bol}}/L_{\text{Edd}}$.

Finally, we assumed the standard accretion disk model by Shakura & Sunyaev (1973) to estimate the maximum black-body temperature T_{max} of the disk assuming it reaches the innermost stable circular orbit:

$$T(r) = \left(\frac{3GM_{\text{BH}}\dot{m}}{8\pi\sigma r^3}\right)^{1/4} \left(1 - \sqrt{\frac{R_{\text{ISCO}}}{r}}\right)^{1/4} \quad (4)$$

where \dot{m} is the AGN accretion rate and $R_{\text{ISCO}} = 6GM_{\text{BH}}/c^2$ is the radius of the innermost stable orbit around the (non-rotating) central SMBH. To find T_{max} , we estimated $\dot{m} = L_{\text{bol}}/\eta c^2$ adopting a radiative efficiency $\eta = 0.057$ for a non-rotating SMBH

³ Estimating M_{BH} with the Denney (2012) relation from the C IV FWHM computed over the entire line profile would yield $(1.0 \pm 0.4) \times 10^7 M_{\odot}$, i.e. a factor of ≥ 2 lower than the SDSS value.

(Novikov & Thorne 1973), and took the maximum value assumed by Eq. 4 along the disk radius for our choice of free parameters.

Table 3. AGN parameters derived from the analysis of the RBS 1332 C IV spectral region.

Quantity	Value	Units
FWHM_{CIV}	1570 ± 90	km s^{-1}
$\lambda L_{\lambda}(1350 \text{ \AA})$	$(2.1 \pm 0.6) \times 10^{44}$	erg s^{-1}
$\lambda L_{\lambda}(1450 \text{ \AA})$	$(2.0 \pm 0.6) \times 10^{44}$	erg s^{-1}
L_{bol}	$(0.8 \pm 0.2) \times 10^{45}$	erg s^{-1}
L_{Edd}	$(2.0 \pm 0.6) \times 10^{45}$	erg s^{-1}
ε_{Edd}	0.4 ± 0.2	—
\dot{m}	0.26 ± 0.07	$M_{\odot} \text{ yr}^{-1}$
M_{BH}	$(1.7 \pm 0.5) \times 10^7$	M_{\odot}
R_{ISCO}	$(1.5 \pm 0.4) \times 10^{13}$	cm
T_{max}	$(1.9 \pm 0.3) \times 10^5$	K

3.2. Parameters of the absorption features associated with the Ly α , N v and C IV transitions

As a next step, we investigated the absorption features associated with the main UV transitions that are present in the RBS 1332 spectrum. To this aim, we first divided the spectrum by the pseudo-continuum obtained by summing all of the emission components derived in the previous steps; then, under the assumption that the AGN emission $F_{\lambda}^{(0)}$ is exponentially absorbed owing to the transport equation (e.g., Rybicki & Lightman 1979):

$$F_{\lambda} = F_{\lambda}^{(0)} \times e^{-\tau_{\lambda}} \quad (5)$$

we empirically modeled the absorption optical depth τ_{λ} as a sum of Gaussian profiles:

$$\tau_{\lambda} = \sum_i A_i \exp\left[-\frac{(\lambda - \lambda_i)^2}{2\sigma_i^2}\right] \quad (6)$$

The inspection of the Ly α , N v and C IV spectral regions revealed that the Ly α absorption troughs are both formed by two narrower components; also the intermediate-velocity N v absorption is double, whereas the C IV troughs exhibit simpler single shapes. Therefore, we adopted four Gaussian profiles for both the Ly α and N v absorption, and only three for the C IV one, for a total of 11 components.

We fitted this model to the normalized RBS 1332 spectrum, leaving all the absorption parameters free to vary. The best fits obtained in this way are shown in Fig. 6 for each spectral region, along with the corresponding χ^2 and $\nu_{\text{d.o.f.}}$ values. From the fit results, we computed the absorption equivalent widths EW_i , velocity shifts Δv_i and widths FWHM_i of each component, along with the corresponding 1σ uncertainties; we report such values in Tab. 4, numbering each absorption and grouping troughs associated to each transition according to their velocity shift (from blue to red). This led us to establish the following relations:

- the most detached “blue” troughs (System 1) all have velocity shifts in the range from -1200 km s $^{-1}$ to -800 km s $^{-1}$, with FWHMs in the range $300 \div 600$ km s $^{-1}$;
- the “bluer” intermediate troughs (System 2) have velocity shifts of $-500 \div -600$ km s $^{-1}$, with comparable FWHMs of $550 \div 650$ km s $^{-1}$ and also similar EWs (around ~ 40 km s $^{-1}$ for both the Ly α and the N v); interestingly, the C IV transition does not show this absorption component;
- the “redder” intermediate troughs (System 3) exhibit similar velocity shifts of $-150 \div -250$ km s $^{-1}$, but more variegated FWHMs that range from ~ 250 km s $^{-1}$ up to ~ 1600 km s $^{-1}$;
- the “red” troughs (System 4) also have mixed properties in terms of both velocity shifts (from ~ 0 to ~ 600 km s $^{-1}$) and spread (FWHMs from ~ 400 km s $^{-1}$ to ~ 1200 km s $^{-1}$), being joined by mostly the fact of having positive velocity shifts with respect to the transition wavelength and by very similar EWs (all around ~ 100 km s $^{-1}$).

Overall, the parameters reported in Table 4 highlight how the analyzed absorption features exhibit intermediate velocity properties between broad (BALs; e.g., Lynds 1967; Weymann et al. 1991) and narrow absorption lines (NALs; e.g., Reynolds 1997; Elvis 2000), in line with those of the so-called mini-BALs (see e.g. Perna et al. 2024, and refs. therein). This interpretation is further supported by the lack of consistent variability over a maximum time interval $\Delta t \sim 13$ days between the UV observations, corresponding to ~ 11.6 days in the rest frame; based on this evidence, under the assumption of a photoionization-driven absorption variability (Barlow et al. 1992; Trevese et al. 2013), we have been able to put an upper limit on the absorber’s electron density n_e as:

$$n_e = \frac{1}{\alpha_{\text{rec}} \Delta t_{\text{rf}}} \quad (7)$$

Assuming e.g. $\alpha_{\text{rec}} = 2.8 \times 10^{-12}$ cm 3 s $^{-1}$ for the C IV troughs (Arnaud & Rothenflug 1985) and $\Delta t_{\text{rf}} > 11.6$ days, we got $n_e < 3.6 \times 10^5$ cm $^{-3}$, consistent with the values typically expected for NAL systems (e.g., Elvis 2000; Saturni et al. 2016).

To further quantify the RBS 1332 absorption properties, we estimated the column densities N_{ion} associated with each trough (e.g., Savage & Sembach 1991). Under the assumption of an optically thin line lying on the linear part of the curve of growth associated to an absorber with full covering fraction, the minimum N_{ion} is related to its EW as (e.g., Mehdipour et al. 2023):

$$N_{\text{ion}}(\text{cm}^{-2}) \approx \frac{1.13 \times 10^{20}}{f \lambda^2} \text{EW}(\text{\AA}) \quad (8)$$

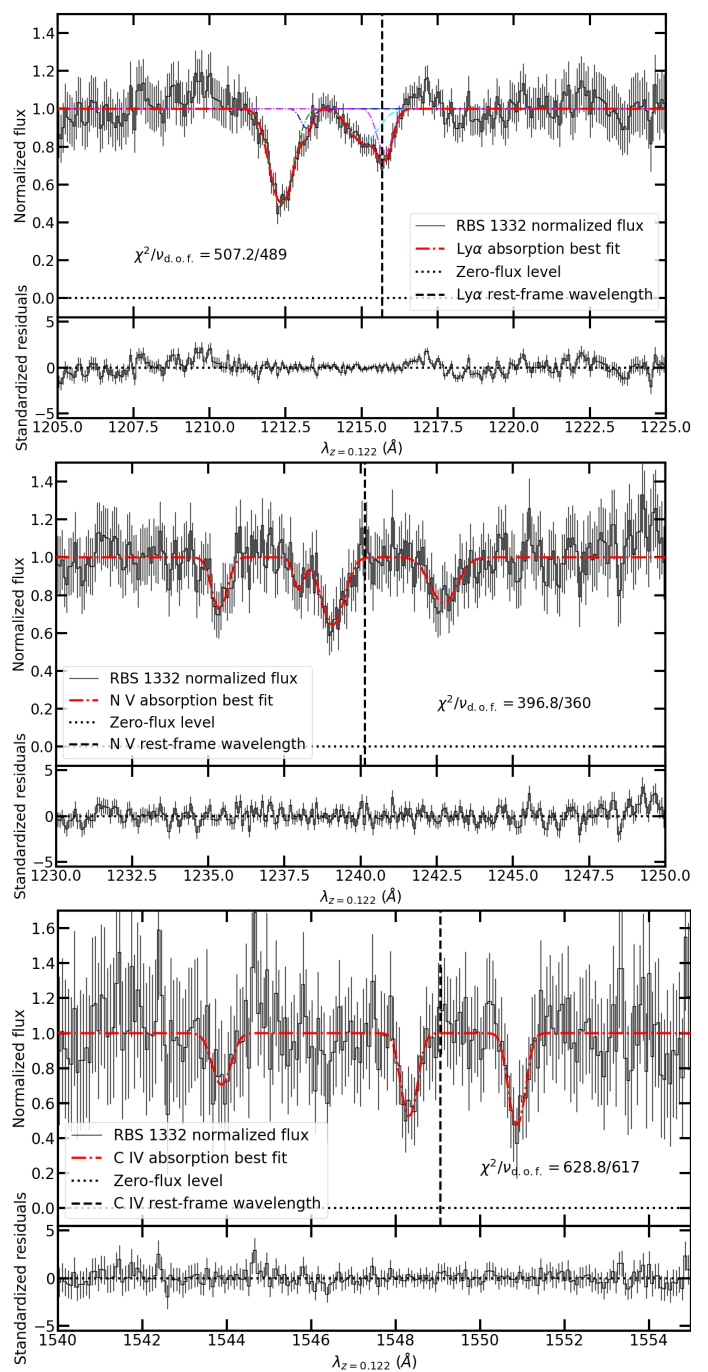


Fig. 6. Fits to the absorption systems (red dot-dashed lines) associated with the RBS 1332 major emission features, along with the corresponding standardized residuals. *Upper panels:* fit to the Ly α absorption features. *Middle panels:* fit to the N v absorption features. *Lower panels:* fit to the C IV absorption features. In all panels, the zero-flux level (dotted lines) is indicated along with the rest-frame position of the relative emission feature (dashed lines).

where f is the oscillator strength and λ the laboratory wavelength of the transition. We retrieved the values of these quantities from the Atomic Spectra Database v5.12 4 (Kramida et al. 2024) provided by the National Institute of Standards and Technology (NIST). Based on the EW values that we found for the Ly α , N v and C IV absorptions, we thus computed the corre-

⁴ Available at <https://www.nist.gov/pml/atomic-spectra-database>.

sponding minimum N_{ion} also reported in Tab. 4. All N_{ion} derived in this way lie in the range $2\text{--}12 \times 10^{13} \text{ cm}^{-2}$, in line with typical column densities found for objects with comparable absorption properties (e.g., Wildy et al. 2016; Mehdipour et al. 2023).

The similarities in the physical properties of these absorption systems hint at their common origin, potentially due to the existence of a clumpy (e.g., Dannen et al. 2020; Ward et al. 2024) ionized outflow that is launched outward of the central engine by radiation pressure (e.g., Murray & Chiang 1995; Proga et al. 2000; Risaliti & Elvis 2010), then slows down and starts falling back into the AGN; alternatively, a scenario in which outflow velocities arise from the scattering-off material in a spiralling inflow (Gaskell & Goosmann 2016) may also work. Further multi-wavelength observations and detailed studies that are able to (i) derive the properties of the RBS 1332 UV absorption from prime principles (e.g., by computing numerical models with the CLOUDY software; Ferland et al. 1998), and (ii) relate them to other observable quantities such as the [O III] $\lambda 5007$ broadening to infer the orientation of the central engine with respect to the line of sight (e.g., Risaliti et al. 2011), are needed to fully understand the physical processes at work behind such features.

Table 4. *Upper section:* parameters of the RBS 1332 absorptions associated to the Ly α , N V and C IV transitions, along with the associated 1σ uncertainties. In all columns, values are expressed in km s^{-1} . *Lower section:* minimum column density of the absorbing ions. In all columns, values are expressed in units of 10^{13} cm^{-2} .

Parameter	Ly α	N V	C IV
EW ₁	98.2 ± 3.0	52.7 ± 2.3	79.9 ± 3.6
EW ₂	41.8 ± 1.8	40.4 ± 1.8	—
EW ₃	129.5 ± 5.5	72.1 ± 2.9	58.4 ± 2.5
EW ₄	94.3 ± 4.2	95.7 ± 3.7	105.4 ± 4.0
Δv_1	-810 ± 10	-1160 ± 10	-1010 ± 10
Δv_2	-600 ± 10	-530 ± 10	—
Δv_3	-150 ± 30	-260 ± 10	-140 ± 10
Δv_4	20 ± 10	630 ± 10	350 ± 10
FWHM ₁	270 ± 10	400 ± 10	610 ± 10
FWHM ₂	650 ± 10	540 ± 10	—
FWHM ₃	1620 ± 40	380 ± 10	250 ± 10
FWHM ₄	410 ± 10	1240 ± 30	1190 ± 20
$N_{\text{ion}}^{(1)}$	5.48 ± 0.17	6.84 ± 0.30	6.81 ± 0.31
$N_{\text{ion}}^{(2)}$	2.33 ± 0.10	5.24 ± 0.23	—
$N_{\text{ion}}^{(3)}$	7.23 ± 0.31	9.35 ± 0.38	4.98 ± 0.21
$N_{\text{ion}}^{(4)}$	5.26 ± 0.23	12.42 ± 0.48	8.98 ± 0.34

4. X-ray Spectral analysis

In this section we will report on the broadband spectral fitting that were performed using XSPEC (Arnaud 1996). During the fitting procedure, the hydrogen column density due to the Milky Way $N_{\text{H}}=7.82 \times 10^{19} \text{ cm}^{-2}$ (HI4PI Collaboration et al. 2016) is always included and kept frozen to the quoted value. When COS and OM data are analysed, extinction is taken into account and we assumed $E(B-V)=0.0067$ (Schlafly & Finkbeiner 2011). We assumed the standard cosmology Λ CDM framework with

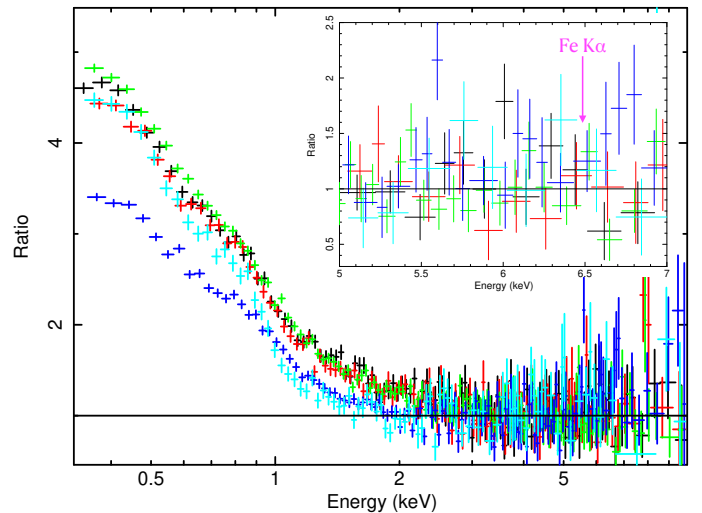


Fig. 7. Ratios of the XMM-Newton data to a power-law fitting the 3-10 keV energy range. A variable and remarkable soft-excess is clearly present below 3 keV, while no hints of a Fe K α emission line are observed.

$H_0=70 \text{ km s}^{-1} \text{ Mpc}^{-1}$, $\Omega_{\text{m}}=0.27$ and $\Omega_{\lambda}=0.73$. The X-ray emission of RBS 1332 is dominated by a prominent and variable soft X-ray emission that exceeds the steep ($\Gamma > 2$) primary continuum. In Fig. 7 we show the residuals to a power-law component fitting only the 3-10 keV energy range. Interestingly, no features ascribable to a Fe K α emission line are observed, see inset in Fig. 7. Previous analysis aimed at characterizing the physical origin of the soft X-ray excess in AGN have focused on X-ray data only. However, such an approach has been found inconclusive as the main competing scenarios give similar best fit quality for the X-ray emission (e.g. García et al. 2019). However, they provide different estimates for the UV emission, thus, in the following, we will directly work on our broadband UV to X-ray dataset.

Testing relativistic reflection:

As stated, our dataset extends down to the UV domain, hence, in the modelling, we need to include any possible contribution of the Broad Line Region (BLR) which is responsible for excess of photons observed around 3000 \AA , the so-called small blue bump (SBB). We considered this spectral component using an additive table within XSPEC that was already presented in Mehdipour et al. (2015). During the fitting procedure, the normalization of the Small Blue Bump was free to vary (but tied among the observations). From the fit we obtained a flux of $F_{0.001\text{--}0.01 \text{ keV}} = (8.7 \pm 0.3) \times 10^{-13} \text{ erg s}^{-1} \text{ cm}^{-2}$ for this component. This flux is quantitatively compatible within the errors with the one obtaining by integrating the differential continuum derived in Sect. 3 from the HST data.

Despite the lack of a significant Fe K α feature, we tested relativistic reflection as the origin of the X-ray soft excess in RBS 1332. At this stage a reflection component cannot be ruled out as the lack of evidence of a Fe K feature can be explained by the presence of an extremely broad Iron line which is hard to detect in limited S/N data. Moreover, very weak Fe K emission line is expected when specific disk properties are met (e.g. high ionization García et al. 2014), or in presence of relativistic effects near a maximally spinning BH (Crummey et al. 2006) or simply by a very soft shape of the X-rays.

Thus, we started modelling the hard X-ray continuum

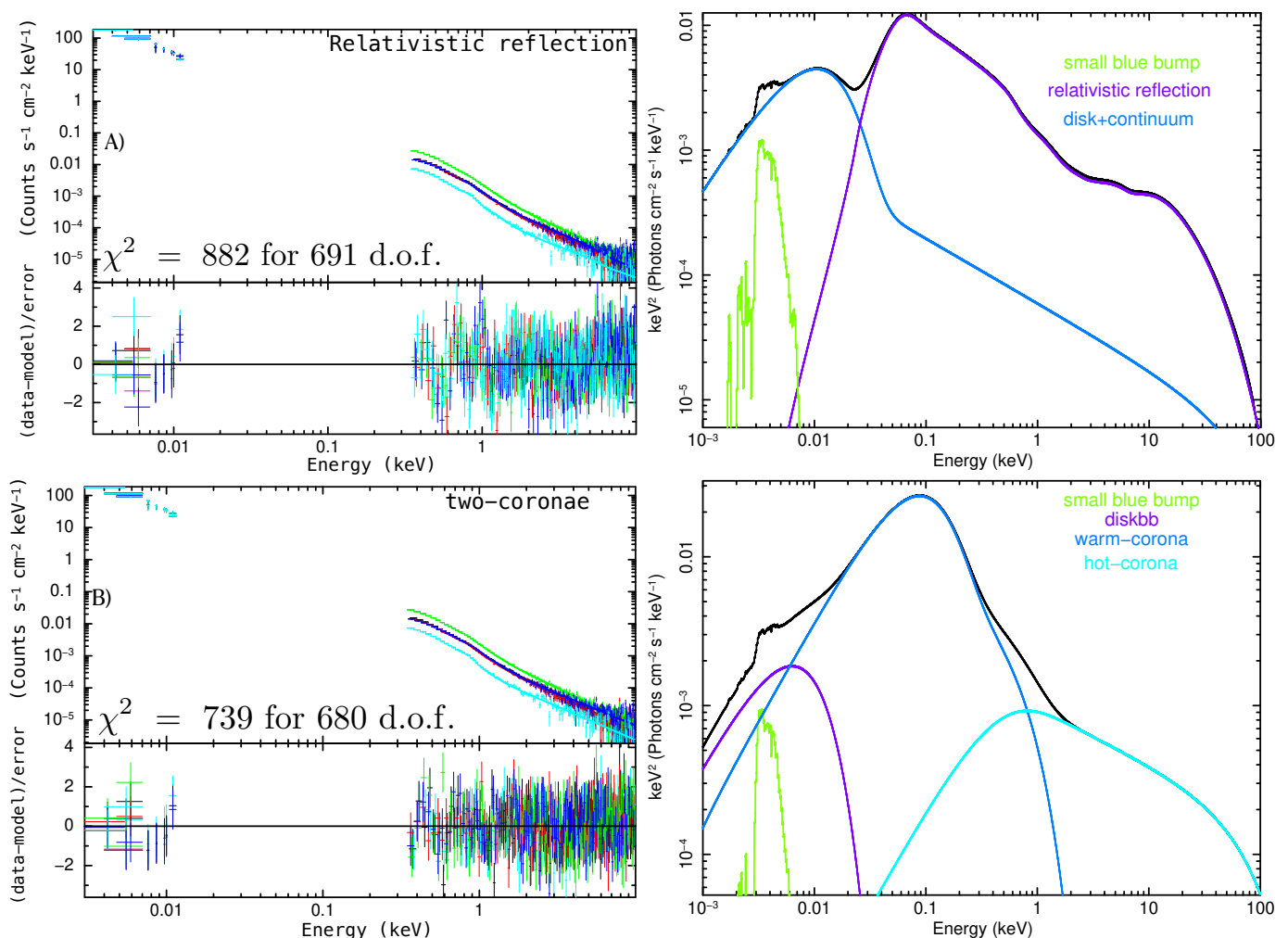


Fig. 8. Top panels: Broadband fit to the OM, COS and EPIC-pn data assuming the soft X-ray excess to be dominated by relativistic reflection (top left). On the top right panel we show the different contributions to the overall emission spectrum of RBS 1332 for each of the model components as inferred from Obs. 1. Bottom panels: Broadband fit of the same dataset assuming the soft X-ray excess to be dominated by a warm Comptonization (left panel). Right panel: the different contribution to the overall emission spectrum of RBS 1332 as derived from the first observation of our observational campaign.

with `THCOMP`, a convolution model meant to replace `NHTCOMP` (Magdziarz & Zdziarski 1995; Zdziarski et al. 1996; Życki et al. 1999). This model describes a Comptonization spectrum by thermal electrons emitted by a spherical source and accounts for a sinusoidal-like spatial distribution of the seed photons, like in `COMPST` (Sunyaev & Titarchuk 1980). `THCOMP` describes both upscattering and downscattering radiation and as a convolution model it can be used to Comptonize any seed photons distribution. In our case, we assumed the seed radiation to emerge from a `DISKBB` component used to provide a standard spectrum from a multi-temperature accretion disk. Within `THCOMP`, it is possible to compute the photon index Γ , the temperature of the seed photons and a covering fraction, $0 \leq cov_{\text{frac}} \leq 1$. When set to 1, all of the seed photons are Comptonized by the plasma while when this below 1, only a fraction of the seed photons is energized. In our computations we left cov_{frac} free to vary. We then linked to this continuum emission a relativistic reflection component using `RELXILLCP` (e.g. García et al. 2014) and assumed the photon index of the two components to be the same. `RELXILLCP`, combines the `XILLVER` reflection code and the `RELLINE` ray tracing code (e.g. Dauser et al. 2016) and returns a spectrum due to irradiation of the accretion disk by an incident

Comptonized continuum. Written in XSPEC notation, this model reads as:

`tbabs × reddn × (SBB + thcomp × diskbb + relxillcp)`.

For each exposure of the monitoring, we calculated the source photon index Γ (linking this parameter between `THCOMP` and `RELXILLCP`), the temperature of the accretion disk (T_{bb} (eV)) and its normalization. For `RELXILLCP`, the ionization parameter $\log \xi$ ($1/\text{erg cm}^{-2} \text{s}^{-1}$) and its normalization were fitted for each exposure. On the other hand, the iron abundance A_{Fe} , the disc inclination incl° , the BH spin (a) and the coronal emissivity (index1) were, instead, fitted tying their values among the observations. The covering fraction of the Comptonizing plasma was also fitted linking its value among the pointings.

This approach led us to a fit statistic $\chi^2=882$ for 691 d.o.f. and we show the corresponding fit and its accompanying quantities in Fig. 8 and Table 5, respectively.

In accordance with this model, the broadband emission of RBS 1332 can be ascribed to a black-body like emission that dominates the FUV and UV wavelengths. No significant changes in its temperature are observed. In this depicted scenario, only a marginal fraction of the photons emitted by the disk are Comp-

Table 5. Best-fit parameters derived for the relativistic reflection scenario. Errors are given at the 90% confidence level for the single parameter of interest.

Relativistic reflection		Obs. 1	Obs. 2	Obs. 3	Obs. 4	Obs. 5
SBB	Norm \dagger ($\times 10^{-3}$)	2.7 \pm 0.1				
redden	E(B-V) \dagger	0.0067				
Tbabs	N $_H$ \dagger ($\times 10^{19}$ cm $^{-2}$)	7.82				
thcomp	Γ	2.52 \pm 0.02	2.52 \pm 0.03	2.55 \pm 0.01	2.41 \pm 0.02	2.51 \pm 0.03
	CF \dagger	7% \pm 4%				
Diskbb	T $_{bb}$ (eV)	4.7 \pm 0.9	4.8 \pm 0.8	3.7 \pm 0.6	4.6 \pm 0.6	5.0 \pm 0.7
	Norm ($\times 10^9$)	1.4 \pm 0.6	1.3 \pm 0.8	2.9 \pm 1.1	1.5 \pm 0.7	1.1 \pm 0.7
relxillcp	incl	(58 \pm 2) $^\circ$				
	index1	>8.85				
	a	>0.997				
	A $_{Fe}$	1.6 \pm 0.3				
	log ξ	3.12 \pm 0.05	3.10 \pm 0.05	3.20 \pm 0.05	3.00 \pm 0.06	2.7 \pm 0.1
	Norm ($\times 10^{-5}$)	2.6 \pm 0.1	2.4 \pm 0.1	4.5 \pm 0.2	2.4 \pm 0.1	1.7 \pm 0.2

tonized by the hot corona ($\text{cov}_{frac} \sim 7\%$) and the X-rays can be mainly ascribed to extreme relativistic reflection. A very steep emissivity is found ($\text{index1} > 8.85$), this implying the Comptonizing plasma to be very close to the maximally rotating SMBH ($a > 0.997$).

Testing warm Comptonization:

Alternatively to blurred ionized reflection we tested the two-coronae model (e.g. Petrucci et al. 2018; Kubota & Done 2018). Within this framework, the broadband emission spectrum of AGN is accounted for by distinct emitting zones, a standard accretion disk; a warm Comptonizing plasma; and the inner hot corona. In particular the disk can be either non-dissipative and in this case be fully covered by the warm corona or, instead, contribute to the overall flux of the source. In this second scenario the warm corona is assumed to be patchy and part of the energy dissipated in the disk leaked through the warm coronal region. The warm corona is defined as an optically thick geometrically thin medium in which Comptonization is the dominant cooling mechanism (Petrucci et al. 2018, 2020) while the hot corona is the one standard depicted in the two-phase model. We thus modified our previously adopted test model as follows:

$$\text{tbabs} \times \text{reddend} \times (\text{SBB} + \text{thcomp}_W \times \text{diskbb} + \text{nthcomp}_H).$$

Thus we model the broadband emission spectrum of RBS 1332 assuming an outer disk for which we compute its temperature (T_{bb}) linking its value among the observations. The normalization $\text{Norm}_{\text{disk}}$ is instead derived in each observation. Then, we assume the soft X-rays emerging from a closer region in which a fraction of disk photons are Comptonized ($\text{thcomp}_W \times \text{diskbb}$). For this second component we fitted the photon index, the temperature and normalization of the disk photons, the covering fraction of the warm corona and its normalization. Finally, for the hot corona we assumed that the seed photons cooling it are only those from the warm component ($T_{bb}^H = kT_{\text{warm}}$). We fixed the hot corona temperature to a constant value of $kT = 50$ keV, in agreement with average estimates (e.g. Middei et al. 2019a; Kamraj et al. 2022). Thus, we only fitted the photon index Γ_H and the model normalization. These simple steps led us to a best-fit of $\chi^2/\text{d.o.f.} = 739/680$ shown in Fig. 8 bottom panels.

This best-fit to the data agrees with the optical-to-X-rays emission of RBS 1332 emerging from three distinct components. A hot corona with a soft spectral index ($\Gamma_{\text{hard}} \sim 2.2$). Then a warm

corona region characterized by an average spectral index steeper than the primary continuum ($\Gamma_{\text{soft}} \sim 2.65$) and an average temperature $kT_{\text{warm}} \sim 0.2$ keV. These values can be translated into a Thompson opacity⁵ of $\tau_{\text{warm}} \sim 30$. These inferred parameters for the warm corona are in full agreement with the bulk of measurements reported by Petrucci et al. (2018). Finally, we add a standard disk responsible for the optical emission, part of which is Comptonized by the hot corona. In Tab. 7 we show the relative flux of the various components used to model the UV-to-X-ray spectra of RBS 1332 and in Fig. 9 we show the corresponding emission components. The best-fit temperature of the accretion disk $T_{\text{in}} \sim 1.2$ eV is a factor of ~ 10 less than the T_{max} reported in Tab. 3; however, we remark that T_{max} is just the upper limit to the range of BB temperatures achievable by an optically thick and geometrically thin accretion disk (Shakura & Sunyaev 1973). Furthermore, the T_{max} derived from the UV spectral analysis is only a factor of ~ 2 lower than the average $T_{bb} \sim 30$ eV – corresponding to $\sim 3.5 \times 10^5$ K – found for the BB component of the warm corona. Based on these evidences, we conclude that all the gas temperatures obtained from the UV and X-ray analyses are in line with the typical values expected for accretion-powered AGN activity.

In the context of the two-coronae model we find that the disc component is fairly constant during the campaign while both the hard power-law and the warm corona changes in flux by a compatible amount. As a final test, we fit the broadband data of RBS 1332 using the model AGNSED, (Done et al. 2012; Kubota & Done 2018). Within this model, the three distinct emitting zones (outer disk, warm corona and hot corona) are energetically coupled and assumed to be radially stratified. The first one emits as a standard disc black body (BB) from R_{out} to R_{warm} , as warm Comptonization from R_{warm} to R_{hot} (see Petrucci et al. 2018, 2020, for details on this region) and, below R_{hot} down to R_{ISCO} as the typical geometrically thick, optically thin electron distributions expected to provide the AGN hard X-ray continuum (Haardt & Maraschi 1993). Radii are in units of gravitational radii R_g . In the fitting procedure, we calculated the hard and the warm corona photon indices (Γ_{hard} and Γ_{soft}), the warm coronal temperature kT_e (keV) while the hard coronal

⁵ This computation relies on the equation $\tau = (2.25 + 3/(\theta \times ((\Gamma + 0.5)^2 - 2.25)))^{1/2} - 1.5$ in which a spherical geometry of the Comptonizing medium is assumed. This comes from an internal routine within the NTHCOMP model.

Table 6. Best-fit parameters corresponding to the two-coronae fitting model. Fluxes and luminosity are the observed ones.

warm Comptonization		Obs. 1	Obs. 2	Obs. 3	Obs. 4	Obs. 5
SBB	Norm [†] ($\times 10^{-3}$)	2.7 \pm 0.1				
redden	E(B-V) [†]	0.0067				
Tbabs	N _H [†] ($\times 10^{19}$ cm ⁻²)	7.82				
diskbb	T _{in} [†] (eV)	1.2 \pm 0.2				
	Norm ($\times 10^{11}$)	1.0 \pm 0.4	1.0 \pm 0.3	1.2 \pm 0.3	1.1 \pm 0.4	0.9 \pm 0.3
warm corona	Γ _{soft}	2.65 \pm 0.20	2.52 \pm 0.19	2.41 \pm 0.15	2.59 \pm 0.09	2.48 \pm 0.16
	kT _e (keV)	0.19 \pm 0.03	0.19 \pm 0.02	0.18 \pm 0.01	0.24 \pm 0.02	0.17 \pm 0.01
	τ _{wc}	30 \pm 3	32 \pm 6	35 \pm 4	28 \pm 3	35 \pm 3
	cov _{frac}	0.18 \pm 0.07	0.15 \pm 0.06	0.19 \pm 0.05	0.17 \pm 0.04	0.19 \pm 0.08
	T _{bb} (eV)	35 \pm 2	33 \pm 3	39 \pm 2	33 \pm 2	23 \pm 7
	Norm ($\times 10^6$)	3.2 \pm 0.8	3.7 \pm 1.2	2.2 \pm 0.7	3.8 \pm 0.8	11 \pm 5
hot corona	Γ _{hot}	2.39 \pm 0.09	2.34 \pm 0.09	2.36 \pm 0.03	2.01 \pm 0.09	2.1 \pm 0.1
	Norm ($\times 10^{-4}$)	9.5 \pm 1.0	8.51 \pm 0.8	15.1 \pm 0.9	6.6 \pm 0.8	3.0 \pm 0.3
	L _{2-10 keV} ($\times 10^{43}$ erg s ⁻¹)	5.6 \pm 0.2	5.3 \pm 0.2	9.1 \pm 0.2	6.7 \pm 0.3	2.5 \pm 0.3
	F _{0.5-2 keV} ($\times 10^{-12}$ erg cm ⁻² s ⁻¹)	3.5 \pm 0.3	3.2 \pm 0.3	5.9 \pm 0.4	3.5 \pm 0.3	1.5 \pm 0.6
	F _{2-10 keV} ($\times 10^{-12}$ erg cm ⁻² s ⁻¹)	1.4 \pm 0.2	1.3 \pm 0.1	2.3 \pm 0.2	1.7 \pm 0.1	0.7 \pm 0.1

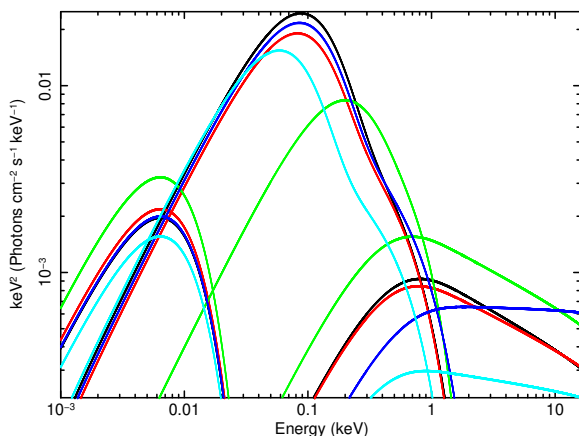

Fig. 9. The three components shaping the broadband emission of RBS 1332 are shown for each observation of the campaign.

Table 7. Fluxes for the different emission components adopted to model the broadband emission of RBS 1332 assuming the two-coronae model.

	diskbb (0.001-0.3 keV)	warm corona 0.3-2 keV	hot corona 2-10 keV
Obs. 1	-11.20 \pm 0.02	-11.20 $^{+0.12}_{-0.02}$	-11.91 \pm 0.09
Obs. 2	-11.19 \pm 0.02	-11.40 \pm 0.05	-11.87 \pm 0.02
Obs. 3	-11.19 \pm 0.02	-11.10 \pm 0.02	-11.63 \pm 0.01
Obs. 4	-11.19 \pm 0.02	-11.30 \pm 0.05	-11.75 \pm 0.02
Obs. 5	-11.19 \pm 0.02	-11.67 \pm 0.03	-12.18 \pm 0.03

temperature was kept to a fixed value of 50 keV. A co-moving distance of 539 Mpc was derived from the redshift and fixed in the model. We assumed a SMBH mass of $\log M_{BH}=7.2\pm 0.2$, based on our computations from the UV spectrum in Sect. 3. We set the scale height for the hot Comptonization component, HT_{max} to 10 gravitational radii R_g , this mimicking a spherical Comptonizing plasma of similar radius. Finally, we assumed a disk inclination of 30° and a spin of 0.5. This led us to a

Table 8. Radial extension in gravitational radii derived from AGNSED.

	Obs. 1	Obs. 2	Obs. 3	Obs. 4	Obs. 5
R _{hot}	12 \pm 2	10 \pm 2	12.5 \pm 0.5	9 \pm 1	7 \pm 1
R _{warm}	200 \pm 35	190 \pm 80	320 \pm 40	175 \pm 30	80 \pm 20
log \dot{m}	-0.41 \pm 0.03	-0.42 \pm 0.07	-0.27 \pm 0.01	-0.42 \pm 0.03	-0.58 \pm 0.04

best-fit of $\chi^2=785$ for 691 d.o.f., fully compatible with the one previously obtained. The spectral index of the hot and warm Comptonization regions are in good agreement with those in Table 6 found in the previous warm Comptonization fit. This fit provides estimates of the size of the different regions of emission. The hot corona appears quite compact ($\sim 10 R_g$), while the warm Comptonization area extends up to $\sim 200 R_g$. We note however variations of this radius R_{warm} of a factor 4 in the 5 observations while the hot coronal region remains more constant. The derived Eddington ratio is in the range is between $\sim 25 - 55\%$ Eddington.

Warm corona or relativistic reflection?

We complement the analyses presented in previous Sect.s 4.1 and 4.2 testing reXCOR⁶ (Xiang et al. 2022; Ballantyne et al. 2024), a spectral model that self-consistently calculates the effects of both ionized relativistic reflection (incorporating the light bending and line's blurring) and the emission from a warm corona. Within reXCOR, the accretion power released in the inner regions of the accretion disk ($<400 r_g$) is distributed among a hot corona (for which a lamppost geometry is assumed), a warm corona and the accretion disk itself. The model reXCOR accounts for a plethora of shapes for the soft X-ray excess that depends on the amount of energy dissipated either by the lamppost or the warm corona.

This model can be used in XSPEC as additive tables that were computed for fixed values of BH spin (0.9,0.99), lamppost height ($5 R_g, 20 R_g$) and Eddington ratio (1%,10%). Up to 5 parameters can be fitted in these tables: the fraction of the

⁶ reXCOR is freely available for spectral fitting using XSPEC at the webpage https://github.com/HEASARC/xspec_localmodels/tree/master/reXcor.

Table 9. Results of the reXCOR model on the RBS 1332 dataset.

	Obs. 1	Obs. 2	Obs. 3	Obs. 4	Obs. 5
Γ	>2.19	2.18±0.01	2.18±0.01	>2.19	>2.19
f_x	0.02±0.01	<0.06	<0.02	0.05±0.01	>0.14
h_f	0.76±0.01	0.65±0.06	0.76±0.01	0.71±0.02	0.55±0.05
τ	>29	21±4	23±3	>28.6	27±2

accretion flux dissipated in the lamppost (f_x), the photon index of the power-law continuum (Γ), the fraction of the accretion flux dissipated in the warm corona (h_f); the warm corona opacity τ , and the model normalization. Then, we tested on our dataset the following XSPEC model:

$$\text{tbabs} \times \text{reddend} \times (\text{diskbb} + \text{nthcomp} + \text{reXcor}(\lambda = 0.1, a = 0.99, h = 5r_g)).$$

We fitted the temperature of the `DISKBB` component linking its value among the observations while its normalization was computed for each dataset. The fraction of the energy dissipated in the lamppost, the warm corona as well as the opacity of this second component and the model normalization were free to vary and fitted for each epoch. We tied the photon index of `reXCOR` to the one of `nthcomp` and computed it. Concerning `nthcomp`, we assumed its T_{bb} temperature to be the same as the disk while the temperature of the hot electron were fixed to 50 keV. We started fitting the `reXCOR` table considering the full *XMM-Newton* band, but due to the limited gamma range ($1.5 < \Gamma < 2.2$) allowed in the model, it struggles to account for the very first soft bins of the spectra. Consequently, we excluded data below 0.5 keV and refitted the spectra, obtaining a better fit statistic $\chi^2 = 760/663$, which is statistically compatible with the one obtained with the two-coronae model. We found that our choice of ignoring data below 0.5 keV does not modify the best fit values for the fraction of energies dissipated in the lamppost or the warm corona. For the sake of simplicity, in Table 9 we only report the quantities derived for the `reXCOR` table, as the other parameters are consistent within the errors with the previously obtained values.

The use of the `reXCOR` model supports the interpretation that the soft X-ray excess is mainly due to inverse-Compton scattering. In fact, for each exposure, the fraction of accretion power dissipated within the warm corona is several times greater than the cooling due to the lamppost.

5. Discussion and Conclusions

We have reported on the first *HST/XMM-Newton* monitoring campaign of the US-NLSy1 galaxy RBS 1332. In the following, we will summarize and discuss our findings.

Variability properties: In the observations the source showed significant flux variability of about 30% on hourly timescales and up to a factor of 4 in about 10 days (see Fig.1). The amount of changes is compatible between the soft (0.5-2 keV) and the hard (2-10 keV) X-rays bands, as no significant spectral changes are witnessed during the exposures. Moreover, neither the UV nor the FUV data seem to vary during the observational campaign (see Fig. 2).

Given the compatible flux observed in the soft X-rays and ultraviolet bands (e.g. Table 7), one could expect the variable soft X-rays to illuminate the outer disc and induce variability in the optical/UVs. In particular, the X-ray reprocessing would cause optical/UV reverberation lags as observed in long and

richly sampled light curves of AGN (e.g. Mason et al. 2002; Arévalo et al. 2005; Alston et al. 2013; Lohfink et al. 2014; Edelson et al. 2015; Buisson et al. 2017; Edelson et al. 2019; Cackett et al. 2023). The lack of variability we observe in the optical/UV bands can be explained by the short timescales investigated here, down to which X-rays variations are likely smeared in the outer disc this weakening any signal associated to reverberation (e.g. Smith & Vaughan 2007; Robertson et al. 2015; Kammoun et al. 2021). Any possible reverberated signal would, in fact, be diluted by the intrinsic UV emission. See Jin et al. (2017b) for a thorough discussion on this subject.

Black hole mass estimates: The significant variability of the X-ray light curve can be used to estimate the supermassive black hole mass. Both long and short term X-ray variability was found to be anti-correlated with the AGN's luminosity and black hole mass (Barr & Mushotzky 1986; Green et al. 1993; Lawrence & Papadakis 1993; Markowitz et al. 2003; Papadakis 2004; McHardy et al. 2006; Vagnetti et al. 2016; Paolillo et al. 2023). Thus, we computed the light curves of RBS 1332 for all the available observations, also including the archival (obs. ID.s 0741390201 and 0741390401) and extracted all the 2-10 keV light curves with a time bin of 500 s. Then, we calculated in each 20 ks-long segment the normalized excess variance (Vaughan et al. 2003), found to be $\sigma_{\text{nx}}^2 = 0.020 \pm 0.009$. Using the relations by Ponti et al. (2012), Tortosa et al. but see also 2023 this quantity yields to a BH mass $M_{\text{BH}} = (7.4 \pm 1.0) \times 10^6 M_{\odot}$. This estimate, that is compatible with previous values using the $L_{5100\text{\AA}}$ and $\text{FWHM}_{\text{H}\beta}$ (see discussion in Xu et al. 2021), is about a factor of 2 smaller than the one inferred from the FUV analysis in Sect. 3.1 or with the single epoch estimate by Wu & Shen (2022). Considering an average value for the 2-10 keV luminosity and adopting the bolometric correction by Duras et al. (2020), we obtain a bolometric luminosity of $L_{\text{bol}} = 8.4 \times 10^{44} \text{ erg s}^{-1}$. This value, coupled with the BH mass derived from the normalized excess variance leads to an Eddington ratio of 90%, about a factor of 2 larger than the one derived from analysis of the FUV spectrum.

The discrepancy between the two values of Eddington ratio can be easily reconciled by the fact that objects with high accretion rates (super-Eddington accreting massive black holes, SEAMBHs) – from significant Eddington fractions to the super-Eddington regime – have been found to possess smaller broad-line region (BLR) sizes with respect to normal quasars (Du et al. 2015), probably related to altered disk and torus geometries. This in turn implies a higher BLR velocity dispersion, and thus a systematic overestimation of the M_{BH} value derived from single-epoch relations in the case of SEAMBHs. Hence, our difference in the M_{BH} values could be easily ascribed to accretion processes close to the Eddington limit powering the RBS 1332 central engine and shaping its internal structure accordingly (see also Jin et al. 2017b). We note that our results, with the exception of AGNSED do not depend on the BH mass and that, irrespectively of the value for the BH mass we may adopt, RBS 1332 is compatible with being efficiently accreting matter.

Properties of the UV absorption features: The main UV high-ionization transitions – Ly α , N V $\lambda 1241$ and C IV $\lambda 1549$ – all show absorption features extended over a wide range of velocities, spanning $\sim 3200 \text{ km s}^{-1}$ from $\sim -1500 \text{ km s}^{-1}$ to $\sim 1700 \text{ km s}^{-1}$. These features do not vary over a time span of ~ 11.6 rest-frame days, implying electron densities $n_e < 3.6 \times 10^5 \text{ cm}^{-3}$ under the assumption of photoionization-driven absorption vari-

ability (Barlow et al. 1992; Trevese et al. 2013). Despite their moderate EWs (from $\sim 40 \text{ km s}^{-1}$ to $\sim 130 \text{ km s}^{-1}$, corresponding to minimum column densities of $2\text{--}12 \times 10^{13} \text{ cm}^{-2}$), the presence of such troughs together with the evidence of blue-shifted emission-line wings associated with forbidden transitions (see e.g. Saturni et al. 2021) points at the existence of a mildly ionized outflow powered by the RBS 1332 central engine, that can be further studied with dedicated investigations on its physical properties and geometry.

Such winds are ubiquitous in AGN at several redshifts (e.g., Kakkad et al. 2016, 2018) and luminosities (e.g., Vietri et al. 2018), often extending to the whole host galaxy (e.g., Perna et al. 2015, 2017) and thus playing an important role in regulating AGN activity and star formation by altering the amount of available gas for both these processes (e.g., Cattaneo et al. 2009; Fabian 2012). Investigating with future dedicated studies the nature of the outflow at work in the RBS 1332 environment will therefore be crucial to understand its impact on the host galaxy environment and evolution (e.g., Ciccone et al. 2018).

Spectral modeling and global picture: We tested four different models to account for the multi-epoch UV-to-X-ray data obtained in the context of our monitoring campaign: blurred relativistic reflection, warm Comptonization (also including AGNSED), and a model that combines both (relativistic reflection and warm-Comptonization), *REXCOR*. In the relativistic reflection scenario, the X-ray emission is in fact dominated by reflection, and the observed variability is mostly due to changes of the reflected flux. This could in turn be related to variations in the geometry of the disc-corona; for example, if the corona is a lamp-post source, a variation of the coronal height above the disc imply a variation of in the solid angle subtended by the disc.

However, we find that the the broadband emission spectrum and the soft X-ray excess are statistically best modelled in the framework of the two-coronae model. A similar conclusion was drawn by Xu et al. (2021) using Swift and XMM-Newton archival exposures.

We found the overall emission spectrum of RBS 1332 emerges from three distinct components: i) a fairly constant outer disk ($\leq 200 R_g$) with $T_{\text{disk}} \sim 1 \text{ eV}$; ii) a patchy warm corona Compton up-scattering about $\sim 20\%$ of the underlying seed photons and extending from about $10 R_g$ to $\sim 200 R_g$; iii) a very compact ($\leq 10 R_g$) hot corona with a soft spectrum. The physical and geometrical parameters of the hot corona are moderately variable during the campaign, as indicated by the fits with AGNSED and *REXCOR*. Also the radial extension of the warm corona shows a significant variability and is positively correlated with the accretion rate, while there is no clear trend with its temperature or optical depth. The same results were obtained by Palit et al. (2024) for a sample of Seyfert galaxies. Despite the extreme soft X-ray excess observed in this source, its photon index, the temperature and the opacity are fairly standard when compared with results from other monitoring campaigns (Ursini et al. 2018; Middei et al. 2018; Porquet et al. 2018; Middei et al. 2019b; Ursini et al. 2020; Middei et al. 2020), archival studies (Petrucci et al. 2018, 2020; Xiang et al. 2022; Ballantyne et al. 2024; Palit et al. 2024) and distant quasars (Marinucci et al. 2022; Vaia et al. 2024).

The extension of the hot corona appears compact ($R_{\text{hot}} \sim 10 R_g$) and characterized by the ultra-soft observed hard power-law ($\Gamma \sim 2.2$). This can be possibly explain by the interplay between a small heating power sustaining the hot corona and the efficient cooling due to the large fraction of seed photons from the warm corona. An other possibility is provided by the presence of a

puffed-up disk-layer between the warm coronal region and the outer disk (Jin et al. 2017b). This bloated layer of matter would be illuminated by the hard continuum, part of which could either pierce through it reaching the outer disk, or being reprocessed thus eventually producing a weak reflection signal.

Finally, although limited by the moderate parameter range in the available *REXCOR* tables, we found that the soft X-ray excess in RBS,1332 is primarily attributable to warm Comptonization with reprocessing of the primary continuum playing only a marginal role. This analysis, along with the findings by Jin et al. (2017a) further supports the two-coronae model as a viable explanation for the multiwavelength emission spectrum of extreme AGN like the US-NLSy galaxies.

Acknowledgements. We thank the anonymous referee for their thorough reading of the manuscript. RM acknowledges Ioanna Psaradaki for insightful discussions on the UV spectra and acknowledges financial support from the ASI-INAF agreement n. 2022-14-HH.0. SB is an overseas researcher under the Postdoctoral Fellowship of Japan Society for the Promotion of Science (JSPS), supported by JSPS KAKENHI Grant Number JP23F23773. This work relies on archival data, software or online services provided by the Space Science Data Center – ASI, and it is based on observations obtained with XMM-Newton, an ESA science mission with instruments and contributions directly funded by ESA Member States and NASA. POP and MC acknowledges financial support from the High Energy french National Programme (PNHE) of the National Center of Scientific research (CNRS) and from the french spatial agency (CNES). BDM acknowledges support via Ramón y Cajal Fellowship (RYC2018-025950-I), the Spanish MINECO grants PID2022-136828NB-C44 and PID2020-117252GB-I00, and the AGAUR/Generalitat de Catalunya grant SGR-386/2021.

References

- Alston, W. N., Vaughan, S., & Uttley, P. 2013, *MNRAS*, 435, 1511
 Arévalo, P., Papadakis, I., Kuhlbrodt, B., & Brinkmann, W. 2005, *A&A*, 430, 435
 Arnaud, K. A. 1996, in *Astronomical Society of the Pacific Conference Series*, Vol. 101, *Astronomical Data Analysis Software and Systems V*, ed. G. H. Jacoby & J. Barnes, 17
 Arnaud, M. & Rothenflug, R. 1985, *A&AS*, 60, 425
 Bade, N., Fink, H. H., Engels, D., et al. 1995, *A&AS*, 110, 469
 Ballantyne, D. R., Sudhakar, V., Fairfax, D., et al. 2024, *MNRAS*, 530, 1603
 Barlow, T. A., Junkkarinen, V. T., Burbidge, E. M., et al. 1992, *ApJ*, 397, 81
 Barr, P. & Mushotzky, R. F. 1986, *Nature*, 320, 421
 Bianchi, S., Guainazzi, M., Matt, G., Fonseca Bonilla, N., & Ponti, G. 2009, *A&A*, 495, 421
 Blanton, M. R., Bershad, M. A., Abolfathi, B., et al. 2017, *AJ*, 154, 28
 Boroson, T. A. & Green, R. F. 1992, *ApJS*, 80, 109
 Buisson, D. J. K., Lohfink, A. M., Alston, W. N., & Fabian, A. C. 2017, *MNRAS*, 464, 3194
 Cackett, E. M., Gelbord, J., Barth, A. J., et al. 2023, *ApJ*, 958, 195
 Cattaneo, A., Faber, S. M., Binney, J., et al. 2009, *Nature*, 460, 213
 Ciccone, C., Brusa, M., Ramos Almeida, C., et al. 2018, *Nature Astronomy*, 2, 176
 Crummy, J., Fabian, A. C., Gallo, L., & Ross, R. R. 2006, *MNRAS*, 365, 1067
 Dannen, R. C., Proga, D., Waters, T., & Dyda, S. 2020, *ApJ*, 893, L34
 Dauser, T., García, J., Walton, D. J., et al. 2016, *A&A*, 590, A76
 Denney, K. D. 2012, *ApJ*, 759, 44
 Done, C., Davis, S. W., Jin, C., Blaes, O., & Ward, M. 2012, *MNRAS*, 420, 1848
 Du, P., Hu, C., Lu, K.-X., et al. 2015, *ApJ*, 806, 22
 Duras, F., Bongiorno, A., Ricci, F., et al. 2020, *A&A*, 636, A73
 Edelson, R., Gelbord, J., Cackett, E., et al. 2019, *ApJ*, 870, 123
 Edelson, R., Gelbord, J. M., Horne, K., et al. 2015, *ApJ*, 806, 129
 Elvis, M. 2000, *ApJ*, 545, 63
 Fabian, A. C. 2012, *ARA&A*, 50, 455
 Fabian, A. C., Lohfink, A., Kara, E., et al. 2015, *MNRAS*, 451, 4375
 Ferland, G. J., Korista, K. T., Verner, D. A., et al. 1998, *PASP*, 110, 761
 Gallo, L. 2018, in *Revisiting Narrow-Line Seyfert 1 Galaxies and their Place in the Universe*, 34
 García, J., Dauser, T., Lohfink, A., et al. 2014, *ApJ*, 782, 76
 García, J. A., Kara, E., Walton, D., et al. 2019, *ApJ*, 871, 88
 Gaskell, C. M. & Goosmann, R. W. 2016, *Ap&SS*, 361, 67
 George, I. M. & Fabian, A. C. 1991, *MNRAS*, 249, 352
 Gliozzi, M. & Williams, J. K. 2020, *MNRAS*, 491, 532
 Goodrich, R. W. 1989, *ApJ*, 342, 224
 Green, A. R., McHardy, I. M., & Lehto, H. J. 1993, *MNRAS*, 265, 664

- Green, J. C., Froning, C. S., Osterman, S., et al. 2012, *ApJ*, 744, 60
- Grupe, D., Komossa, S., Leighly, K. M., & Page, K. L. 2010, *ApJS*, 187, 64
- Grupe, D., Wills, B. J., Leighly, K. M., & Meusinger, H. 2004, *AJ*, 127, 156
- Haardt, F. & Maraschi, L. 1991, *ApJ*, 380, L51
- Haardt, F. & Maraschi, L. 1993, *ApJ*, 413, 507
- Hall, P. B., Anosov, K., White, R. L., et al. 2011, *MNRAS*, 411, 2653
- HI4PI Collaboration, Ben Bekhti, N., Flöer, L., et al. 2016, *A&A*, 594, A116
- Jiang, J., Gallo, L. C., Fabian, A. C., Parker, M. L., & Reynolds, C. S. 2020, *MNRAS*, 498, 3888
- Jin, C., Done, C., & Ward, M. 2017a, *MNRAS*, 468, 3663
- Jin, C., Done, C., Ward, M., & Gardner, E. 2017b, *MNRAS*, 471, 706
- Kakkad, D., Groves, B., Dopita, M., et al. 2018, *A&A*, 618, A6
- Kakkad, D., Mainieri, V., Padovani, P., et al. 2016, *A&A*, 592, A148
- Kammoun, E. S., Papadakis, I. E., & Dovčiak, M. 2021, *MNRAS*, 503, 4163
- Kamraj, N., Brightman, M., Harrison, F. A., et al. 2022, *ApJ*, 927, 42
- Kramida, A., Ralchenko, Y., Reader, J., & NIST ASD Team. 2024, NIST Atomic Spectra Database
- Krongold, Y., Binette, L., & Hernández-Ibarra, F. 2010, *ApJ*, 724, L203
- Kubota, A. & Done, C. 2018, *MNRAS*, 480, 1247
- Lawrence, A. & Papadakis, I. 1993, *ApJ*, 414, L85
- Lohfink, A. M., Reynolds, C. S., Vasudevan, R., Mushotzky, R. F., & Miller, N. A. 2014, *ApJ*, 788, 10
- Lynds, C. R. 1967, *ApJ*, 147, 396
- Magdziarz, P. & Zdziarski, A. A. 1995, *MNRAS*, 273, 837
- Malizia, A., Molina, M., Bassani, L., et al. 2014, *ApJ*, 782, L25
- Mallick, L., Alston, W. N., Parker, M. L., et al. 2018, *MNRAS*, 479, 615
- Marinucci, A., Vietri, G., Piconcelli, E., et al. 2022, *A&A*, 666, A169
- Markowitz, A., Edelson, R., Vaughan, S., et al. 2003, *ApJ*, 593, 96
- Mason, K. O., Breeveld, A., Much, R., et al. 2001, *A&A*, 365, L36
- Mason, K. O., McHardy, I. M., Page, M. J., et al. 2002, *ApJ*, 580, L117
- Matzeu, G. A., Nardini, E., Parker, M. L., et al. 2020, *MNRAS*, 497, 2352
- McHardy, I. M., Koerding, E., Knigge, C., Uttley, P., & Fender, R. P. 2006, *Nature*, 444, 730
- Mehdipour, M., Kaastra, J. S., Kriss, G. A., et al. 2015, *A&A*, 575, A22
- Mehdipour, M., Kriss, G. A., Kaastra, J. S., Costantini, E., & Mao, J. 2023, *ApJ*, 952, L5
- Middei, R., Bianchi, S., Cappi, M., et al. 2018, *A&A*, 615, A163
- Middei, R., Bianchi, S., Marinucci, A., et al. 2019a, *A&A*, 630, A131
- Middei, R., Bianchi, S., Petrucci, P. O., et al. 2019b, *MNRAS*, 483, 4695
- Middei, R., Petrucci, P. O., Bianchi, S., et al. 2020, *A&A*, 640, A99
- Middei, R., Petrucci, P. O., Bianchi, S., et al. 2023, *A&A*, 672, A101
- Murray, N. & Chiang, J. 1995, *ApJ*, 454, L105
- Nardini, E., Lusso, E., & Bisogni, S. 2019, *MNRAS*, 482, L134
- Novikov, I. D. & Thorne, K. S. 1973, in *Black Holes (Les Astres Occlus)*, 343–450
- Osterbrock, D. E. 1977, *ApJ*, 215, 733
- Padovani, P., Alexander, D. M., Assef, R. J., et al. 2017, *A&A Rev.*, 25, 2
- Palit, B., Rozanska, A., Petrucci, P. O., et al. 2024, arXiv e-prints, arXiv:2406.14378
- Paolillo, M., Papadakis, I. E., Brandt, W. N., et al. 2023, *A&A*, 673, A68
- Papadakis, I. E. 2004, *MNRAS*, 348, 207
- Perna, M., Arribas, S., Ji, X., et al. 2024, arXiv e-prints, arXiv:2411.13698
- Perna, M., Brusa, M., Cresci, G., et al. 2015, *A&A*, 574, A82
- Perna, M., Lanzuisi, G., Brusa, M., Cresci, G., & Mignoli, M. 2017, *A&A*, 606, A96
- Perola, G. C., Matt, G., Fiore, F., et al. 2000, *A&A*, 358, 117
- Petrucci, P. O., Gronkiewicz, D., Rozanska, A., et al. 2020, *A&A*, 634, A85
- Petrucci, P. O., Paltani, S., Malzac, J., et al. 2013, *A&A*, 549, A73
- Petrucci, P. O., Ursini, F., De Rosa, A., et al. 2018, *A&A*, 611, A59
- Piconcelli, E., Jimenez-Bailón, E., Guainazzi, M., et al. 2004, *MNRAS*, 351, 161
- Ponti, G., Papadakis, I., Bianchi, S., et al. 2012, *A&A*, 542, A83
- Porquet, D., Hagen, S., Grosso, N., et al. 2024, *A&A*, 681, A40
- Porquet, D., Reeves, J. N., Grosso, N., Braito, V., & Lobban, A. 2021, *A&A*, 654, A89
- Porquet, D., Reeves, J. N., Matt, G., et al. 2018, *A&A*, 609, A42
- Proga, D., Stone, J. M., & Kallman, T. R. 2000, *ApJ*, 543, 686
- Reynolds, C. S. 1997, *MNRAS*, 286, 513
- Risaliti, G. & Elvis, M. 2010, *A&A*, 516, A89
- Risaliti, G., Nardini, E., Salvati, M., et al. 2011, *MNRAS*, 410, 1027
- Robertson, D. R. S., Gallo, L. C., Zoghbi, A., & Fabian, A. C. 2015, *MNRAS*, 453, 3455
- Runnoe, J. C., Brotherton, M. S., & Shang, Z. 2012a, *MNRAS*, 427, 1800
- Runnoe, J. C., Brotherton, M. S., & Shang, Z. 2012b, *MNRAS*, 422, 478
- Rybicki, G. B. & Lightman, A. P. 1979, *Radiative processes in astrophysics*
- Saturni, F. G., Bischetti, M., Piconcelli, E., et al. 2018, *A&A*, 617, A118
- Saturni, F. G., Trevese, D., Vagnetti, F., Perna, M., & Dadina, M. 2016, *A&A*, 587, A43
- Saturni, F. G., Vietri, G., Piconcelli, E., et al. 2021, *A&A*, 654, A154
- Savage, B. D. & Sembach, K. R. 1991, *ApJ*, 379, 245
- Schlaflly, E. F. & Finkbeiner, D. P. 2011, *ApJ*, 737, 103
- Shakura, N. I. & Sunyaev, R. A. 1973, *A&A*, 24, 337
- Smith, R. & Vaughan, S. 2007, *MNRAS*, 375, 1479
- Strüder, L., Briel, U., Dennerl, K., et al. 2001, *A&A*, 365, L18
- Sunyaev, R. A. & Titarchuk, L. G. 1980, *A&A*, 86, 121
- Tortosa, A., Bianchi, S., Marinucci, A., Matt, G., & Petrucci, P. O. 2018, *A&A*, 614, A37
- Tortosa, A., Ricci, C., Arévalo, P., et al. 2023, *MNRAS*, 526, 1687
- Trevese, D., Saturni, F. G., Vagnetti, F., et al. 2013, *A&A*, 557, A91
- Turner, M. J. L., Abbey, A., Arnaud, M., et al. 2001, *A&A*, 365, L27
- Ursini, F., Petrucci, P. O., Bianchi, S., et al. 2020, *A&A*, 634, A92
- Ursini, F., Petrucci, P. O., Matt, G., et al. 2018, *MNRAS*, 478, 2663
- Vagnetti, F., Middei, R., Antonucci, M., Paolillo, M., & Serafinelli, R. 2016, *A&A*, 593, A55
- Vaia, B., Ursini, F., Matt, G., et al. 2024, arXiv e-prints, arXiv:2405.13479
- Vanden Berk, D. E., Richards, G. T., Bauer, A., et al. 2001, *AJ*, 122, 549
- Vaughan, S., Edelson, R., Warwick, R. S., & Uttley, P. 2003, *MNRAS*, 345, 1271
- Vestergaard, M. & Peterson, B. M. 2006, *ApJ*, 641, 689
- Vietri, G., Piconcelli, E., Bischetti, M., et al. 2018, *A&A*, 617, A81
- Walton, D. J., Nardini, E., Fabian, A. C., Gallo, L. C., & Reis, R. C. 2013, *MNRAS*, 428, 2901
- Wang, J. & Xu, D. W. 2015, *A&A*, 573, A15
- Ward, S. R., Costa, T., Harrison, C. M., & Mainieri, V. 2024, arXiv e-prints, arXiv:2407.17593
- Weymann, R. J., Morris, S. L., Foltz, C. B., & Hewett, P. C. 1991, *ApJ*, 373, 23
- Wildy, C., Landt, H., Goad, M. R., Ward, M., & Collinson, J. S. 2016, *MNRAS*, 461, 2085
- Wu, Q. & Shen, Y. 2022, *ApJS*, 263, 42
- Xiang, X., Ballantyne, D. R., Bianchi, S., et al. 2022, *MNRAS*, 515, 353
- Xu, X., Ding, N., Gu, Q., Guo, X., & Contini, E. 2021, *MNRAS*, 507, 3572
- Zdziarski, A. A., Johnson, W. N., & Magdziarz, P. 1996, *MNRAS*, 283, 193
- Życki, P. T., Done, C., & Smith, D. A. 1999, *MNRAS*, 309, 561